International Forum on Aeroelasticity and Structural Dynamics
IFASD 2019
9-13 June 2019, Savannah, Georgia, USA

AEROELASTIC LOADS PREDICTIONS USING CFD-BASED REDUCED ORDER MODELS

Philipp Bekemeyer[1], **Tobias Wunderlich**[1], **Stefan Görtz**[1], **Sascha Dähne**[2]

[1]German Aerospace Center (DLR)
Institute of Aerodynamics and Flow Technology
Lilienthalplatz 7, 38108 Braunschweig, Germany
philipp.bekemeyer@dlr.de

[2]German Aerospace Center (DLR)
Institute of Composite Structures and Adaptive Systems
Lilienthalplatz 7, 38108 Braunschweig, Germany

Keywords: Aeroelastic Model Reduction, Computational Fluid Dynamics, Synthetic Modes, Large Transport Aircraft

Abstract: Aircraft loads analysis is an inherently multidisciplinary process since aerodynamic forces, structural deformations and their correlations need to be accounted for. When increasing the fidelity of underlying mono-disciplinary models, such as using computational fluid dynamics for aerodynamic forces, the coupled fluid-structure analysis becomes an increasingly costly process and ultimately limits the applicability within design and optimization. Reduced order models offer an approach to significantly decrease the computational cost needed while retaining the fidelity of the underlying model. This work proposes a reduced order aerodynamic model which can be coupled with varying structural models rather than developing a reduced order aeroelastic model for a fixed aerodynamic and structural model. This enables generating the model without an actual structural model being present and therefore allows the analysis of different structural models of interest without recomputing the aerodynamic model. First, sampling data is computed using computational fluid dynamics based on a few synthetic mode shapes. Second, a proper orthogonal decomposition-based reduced order model is derived for surface deformations and forces. Finally, a least-squares fit for surface deformations given from the current structural model of interest is performed to find proper orthogonal decomposition coefficients while the overall vertical force is constrained to ensure that trimming conditions are met. Results are presented for the LANN wing at transonic flow conditions and a long-range wing-body configuration. While for the former different synthetic modes are applied and the generality of the method is demonstrated by significantly altering the stiffness of the structural model, for the latter case a structural optimization is performed within each coupling step to highlight the adaptivity of the proposed method. Troughout accurate results are predicted showing only minor deviations for resulting surface force, elastic dispacements and optimized surface thicknesses.

1 INTRODUCTION

A significant number of load cases needs to be accounted during aircraft design and optimization and hence, hundreds if not thousands of coupled fluid-structure analysis are necessary. Whereas industry currently relies on low-fidelity, well-established tools such as panel methods and condensed structural models due to low computational cost as their workhorse, increasing

computational resources enable the direct coupling of computational fluid dynamics (CFD) and computational structural dynamics (CSM) solvers at least for a few selected simulations [1]. Especially in the context of multidisciplinary optimization, computational cost of such coupled simulations remains unfeasable when it comes to computing all load cases and usually leads to either lower-fidelity disciplinary tools for loads handling, a downselection of the included load cases and/or other simplifying assumptions such as a fixed structural model [2–7]. Even though such optimizations successfully enhance the design with respect to key values such as fuel consumption and overall aircraft performance, results remain uncertain due to the simplified loads handling.

A promising approach to reduced computational cost of coupled fluid- structure simulations is reduced order modelling (ROM) [8]. Thus a larger number of higher-fidelity load cases during the loads process might become feasible. The arguably most common model reduction technique is proper orthogonal decomposition (POD) which was first used in fluid dynamics to model coherent structures in turbulent flow fields [9]. Combined with the method of snapshots, POD is a powerful tool to obtain small-sized empirical subspaces at limited computational cost [10]. These subspaces can then be exploited to rapidly predict solutions at previously untried conditions using various different techniques such as interpolation and regression methods [11–14], projection-based approaches [15–17] and least-square minimization techniques [18, 19]. Hence, applications within the aerospace community are widespread, ranging from simple airfoils and wings up to aircraft configurations for steady as well as unsteady flow conditions.

Typically steady aeroelastic ROMs have been computed by analyzing a fixed structural and aerodynamic model while varying aerodynamic parameters such as Mach number or altitude [2, 14]. Whereas this has shown promising results for searching the loads envelope it lacks the capability of accounting for changes in the underlying structural model. However, structural changes are an inherent part of a multidisciplinary optimization either by adjusting thicknesses, redistributing fuel and payload masses or even altering the structural topology. Moreover, at early stages of the design, structural properties might be uncertain. For unsteady aeroelastic phenomena such as flutter or limit cycle oscillations structural deformations are routinely described by a linear combination of structural eigenmodes [20]. Rather than directly using these eigenmodes the concept of synthetic or artificial modes has been suggested to adjust to varying structural models [21]. High-fidelity samples are computed for these synthetic modes and the unsteady aeroelastic response is obtained by first matching the actual eigenmodes of the structural model of interest to the synthetic modes and than performing a linear combination of aerodynamic forces. Results have been presented for generalized aerodynamic forces and flutter investigations offering a promising level of accuracy [21–23]. So far, the concept of synthetic modes has not been utilized to rapidly predict high-fidelity-based, steady aeroelastic loads for varying structural models while incorporating trimming constraints.

Herein, the concept of synthetic modes is adapted for static aeroelastic analysis using CFD-based simulations. Synthetic modes are realized by defining a few artificially defined surface deformations to rapidly predict forces for different surface deformations. First, a few samples are computed to construct a POD-based ROM which accounts for changes in surface deformations and target vertical force. Secondly, POD coefficients are determined by performing a least-squares fit on the target surface deformations while the overall vertical force is constrained to ensure that trimming conditions are met. Thirdly, this procedure is coupled with a CSM solver and iteratively converged to a fluid-structure solution which can then be compared

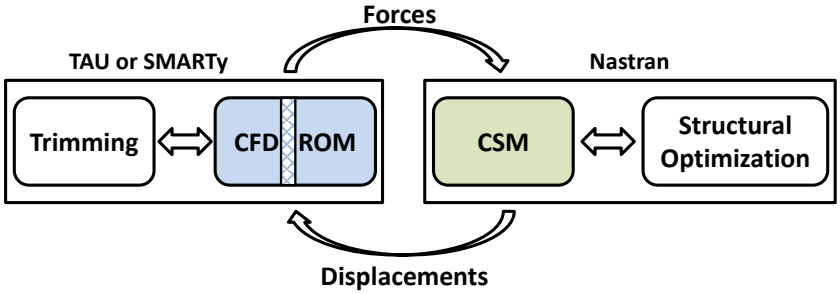

Figure 1: Schematic representation of a loosely coupled fluid-structure simulations framework

to full-order CFD-CSM analysis for different quantities of interest such as force distributions, surface deformations and structural thicknesses. Results are presented for the LANN wing at transonic flow conditions comparing different synthetic mode shapes and showcasing the generality of the method by significantly altering the structural stiffness. Moreover, an aircraft, idealized by a wing-body configuration, is investigated by performing a structural optimization within each fluid-structure coupling step.

2 THEORETICAL FORMULATION

The loosely coupled fluid-structure system is visualized in Fig. 1 showing a separate aerodynamics and structure block. Within each iteration the aerodynamic solver predicts distributed forces on the surface which are then used by the structural solver to compute resulting surface displacements. Based on the new surface shape (baseline plus displacements) the aerodynamic solver predicts updated forces. This iterative scheme is performed until convergence is reached which is typically measured by the relative change in forces and displacements being below a pre-defined threshold. In addition, the aerodynamic forces can be computed under some trimming constraints such as summed vertical force or lift coefficient being equivalent to a pre-set value or pitching moment being zero. During the displacement computation a structural optimization can be performed which adjusts thicknesses to minimize weight while respecting constraints such as maximum stresses. In the following, the focus is on the left-hand-side aerodynamics block which is either provided by a CFD solver or, as suggested here, substituted by a ROM. The requirements for such a model can directly be derived from Fig. 1 and are the accurate prediction of distributed surface forces while accounting for surface displacements and trimming constraints. Hence, if trained accordingly, the same aerodynamic model can be used to rapidly analyze various different structural models.

2.1 Full-Order Aerodynamic Modeling

The governing aerodynamic equations are conveniently written in compact semi-discretized residual form as

$$\frac{d}{dt}\mathbf{w} + \mathbf{\Omega}^{-1}\mathbf{R}(\mathbf{w}, \Delta\mathbf{c}, C_{L,\text{tar}}) = \mathbf{0} \tag{1}$$

where the residual vector $\mathbf{R} \in \mathbb{R}^N$ represents the discretization of the inviscid and viscous flux integrals. The full-order flow solution is denoted by $\mathbf{w} = \left[\mathbf{w}_1, \ldots, \mathbf{w}_{n_p}\right] \in \mathbb{R}^N$ and is spatially discretized over the computational grid of n_p nodes with associated dual-grid cell volumes $\mathbf{\Omega}$. The total number of N flow states is composed of the number of conservative variables per grid point times the number of grid points. For each grid node the vector of unknowns $\mathbf{w}_i$ contains the conservative variables $\mathbf{w}_i = [\rho, \rho\mathbf{v}, \rho E^{\text{t}}, \mathbf{r}^\tau] \in \mathbb{R}^{n_v}$, being ρ the density, $\mathbf{v}$ the velocity vector, E^{t} the total energy, and $\mathbf{r}^\tau$ the set of transported variables associated to the chosen turbulence model such as the turbulent eddy viscosity ν_t. Deformations of the computational

grid, given from the structural solver, are denoted by $\Delta\mathbf{c}$ and the target lift coefficient used for the force trimming is described by $C_{L,\text{tar}}$. A steady, converged solution is obtained once the time-dependent term drops out of Eq. (1), or, equivalently, if the residual term vanishes

$$\mathbf{\Omega}^{-1}\mathbf{R}(\mathbf{w}, \Delta\mathbf{c}, C_{L,\text{tar}}) = \mathbf{0} \tag{2}$$

For a coupled fluid-structure analysis only surface displacements $\Delta\mathbf{c}_\text{s}$ and corresponding surface forces $\boldsymbol{f}_\text{s}$ are relevant and thus only these are accounted for by the proposed ROM. Forces, including pressure and viscous terms, are computed in a post-processing step once a steady solution $\mathbf{w}$ for given surface displacements $\Delta\mathbf{c}_\text{s}$ is found. Note that, the subscript s will be omitted in the following to enhance readability.

2.2 Reduced-Order Aerodynamic Modeling

First, a modal basis needs to be computed which provides a link between surface displacements and surface forces. Within this work POD is applied due to its optimality in representing data with respect to a pre-defined inner product. Also other model reduction techniques such as dynamic mode decomposition or ISOMAP might be suitable. Next, an introduction to POD is given while the interested reader is referred to well established literature for more in-depth, theoretical discussions as well as applications in the field of fluid dynamics [24].

Utilizing the method of snapshots [10], k solutions to Eq. (2) are computed while altering the surface displacements and adjusted the target lift coefficient $C_{L,\text{tar}}$. Surface displacements $\Delta\mathbf{c}$ and resulting forces $\boldsymbol{f}$ are stored as columns in the so-called snapshot matrix

$$S = \left[\begin{pmatrix} \Delta\mathbf{c}_1 \\ \boldsymbol{f}_1 \end{pmatrix}, \begin{pmatrix} \Delta\mathbf{c}_2 \\ \boldsymbol{f}_2 \end{pmatrix}, \ldots, \begin{pmatrix} \Delta\mathbf{c}_k \\ \boldsymbol{f}_k \end{pmatrix} \right] = \begin{pmatrix} S_{\Delta\mathbf{c}} \\ S_{\boldsymbol{f}} \end{pmatrix} \tag{3}$$

for all samples. The unified displacement and force POD basis Φ is then obtained as a linear combination of snapshots

$$\Phi = S\mathrm{V} \tag{4}$$

where the columns of $\mathrm{V} = [\mathbf{v}_1, \mathbf{v}_2, \ldots, \mathbf{v}_k]$ are computed by solving the eigenvalue problem of dimension k

$$S^T S\mathbf{v}_j = \mu_j \mathbf{v}_j \quad \text{for} \quad j = 1, \ldots, k. \tag{5}$$

A singular value decomposition could aclso be applied to the snapshot matrix S, directly yielding the same modal basis Φ. Just as the initial snapshot matrix S, the modal basis Φ can be divided into displacement and force entries

$$\Phi = \begin{pmatrix} \Phi_{\Delta\mathbf{c}} \\ \Phi_{\boldsymbol{f}} \end{pmatrix} \tag{6}$$

Moreover, the basis can be truncated by retaining only the $\tilde{m}$ modes with the highest corresponding eigenvalues μ_j.

Once the modal basis has been computed it can be utilized to predict forces for surface displacements which are not part of the sampling data set $\Delta\boldsymbol{c}_\text{tar}$ since surface displacements and forces can be described as a linear combination of POD modes

$$\begin{pmatrix} \Delta\mathbf{c}^* \\ \boldsymbol{f}^* \end{pmatrix} = \Phi\boldsymbol{a}^* \tag{7}$$

with $\boldsymbol{a}^*$ denoting the corresponding POD coefficients. Various methods are possible to determine the unknown coefficients such as interpolation or residual minimization techniques. Here, coefficients $\boldsymbol{a}^*$ are obtained by solving the constrained minimization problem

$$\begin{aligned} \boldsymbol{a}^* := \quad & \underset{a \in \mathbb{R}^{\tilde{m}}}{\arg\min} \quad \left\| \Phi_{\Delta \boldsymbol{c}} \boldsymbol{a} - \Delta \boldsymbol{c}_{\text{tar}} \right\|_2^2 \\ & \text{s. t.} \quad \boldsymbol{e}^T \Phi_{\boldsymbol{f}_z} \boldsymbol{a} = \boldsymbol{e}^T \boldsymbol{f}_{z,tar} \end{aligned} \tag{8}$$

with $\boldsymbol{e}^T = (1, 1, \ldots, 1)^T$ denoting the unit vector. Multiplication of the equality constraint with this vector on both sides transfers it to a scalar value matching such that the predicted overall vertical force is equivalent to the target vertical force. Because the distributed target vertical force $\boldsymbol{f}_{z,tar}$ is the quantity the ROM is supposed to predict and therefore impossible to guess upfront, the minimization problem is reformulated to

$$\begin{aligned} \boldsymbol{a}^* := \quad & \underset{a \in \mathbb{R}^{\tilde{m}}}{\arg\min} \quad \left\| \Phi_{\Delta \boldsymbol{c}} \boldsymbol{a} - \Delta \boldsymbol{c}_{\text{tar}} \right\|_2^2 \\ & \text{s. t.} \quad \boldsymbol{e}^T \Phi_{\boldsymbol{f}_z} \boldsymbol{a} = F_{z,tar} \end{aligned} \tag{9}$$

by defining a target vertical force $F_{z,tar} = \boldsymbol{e}^T \boldsymbol{f}_{z,tar}$. Note the similarity to a target lift coefficient simulation which is commonly done when solving Eq. (2). In contrast to an interpolation-based approach no additional continuous function needs to be constructed which would limit the solution subspace further and thus introduce additional errors.

2.3 Synthetic Mode Formulation

Two different basis functions for computing synthetic modes are pursued herein which are Chebyshev polynomials and trigonometric functions. Both are used to compute a pre-defined number of synthetic modes equivalent to bending and torsion dominated modes around an elastic axis which is needed as an input. First, the coordinate system is rotated such that the elastic axis becomes the y-axis. Secondly, the rotated wingspan is scaled to a maximum length of one. Thirdly, synthetic deformations are computed for one of the aforementioned basis functions and finally the system is transferred back to its original state. Herein, only results for half-body configurations are shown but the approach can easily extended towards full configurations.

Synthetic deformations $\Delta \boldsymbol{z}_n$ based on a shifted Chebyshev polynomial are given by

$$\Delta \boldsymbol{z}_n \left(\tilde{\boldsymbol{y}} \right) = z_{\max} \delta(\tilde{\boldsymbol{y}}) (-C_n^*(-\tilde{\boldsymbol{y}} + 1) + 1) \tag{10}$$

where $z_{\max}$, $\tilde{\boldsymbol{y}}$ and $\delta(\tilde{\boldsymbol{y}})$ denote the maximum deformation amplitude, the rotated and scaled y-coordinate and a quadratic blending function, respectively. The shifted Chebyshev polynomial $C_n^*(\tilde{\boldsymbol{y}})$ is defined using the recursive function

$$C_{n+1}^*(\tilde{\boldsymbol{y}}) = 2\tilde{\boldsymbol{y}} C_n^*(\tilde{\boldsymbol{y}}) - C_{n-1}^*(\tilde{\boldsymbol{y}}). \tag{11}$$

The shifting and multiplication with minus one moves the maximum excitation to the wingtip and positive upwards. The constant term of the Chebyshev polynomial is omitted since it is equivalent to the undeformed surface. A quadratic blending function $\delta(\tilde{\boldsymbol{y}})$ is applied to ensure no deformations and gradients thereof are present at the wing-root. Other blending functions such as linear and exponential expressions have been tested but not found beneficial in this context. Resulting bending and torsion modes for the wing case are shown in Fig. 2 together with the undeformed surface in blue. The estimated elastic axis is indicated as a red line and corresponds to the one-quarter chord line.

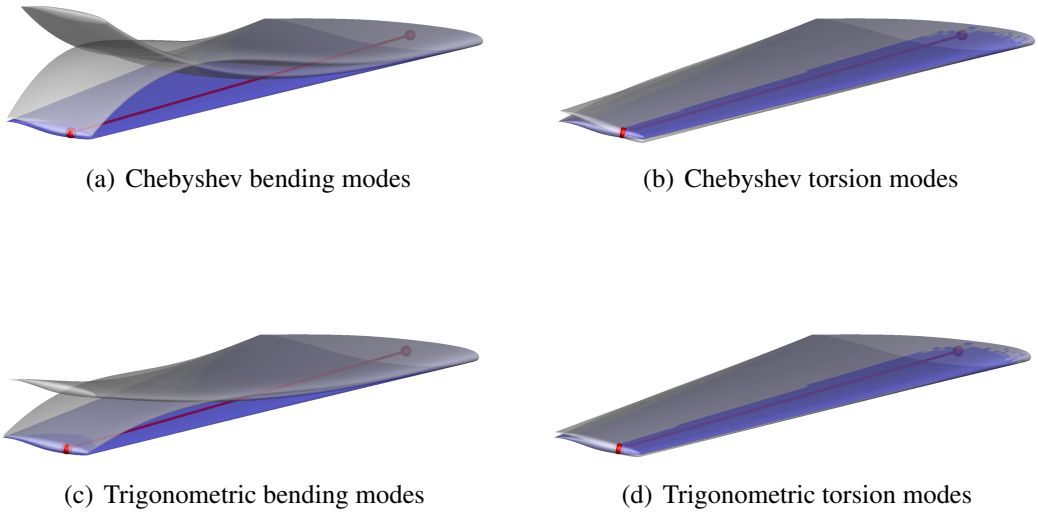

(a) Chebyshev bending modes

(b) Chebyshev torsion modes

(c) Trigonometric bending modes

(d) Trigonometric torsion modes

Figure 2: Generic surface deformations based on Chebyshev-polynomials and trigonometric functions for the wing case. The undeformed surface is given in blue and elastic axis in red.

Synthetic deformations $\Delta \boldsymbol{z}_n$ based on trigonometric functions are computed as

$$\Delta \boldsymbol{z}_n \left(\tilde{\boldsymbol{y}} \right) = z_{\max} \delta(\tilde{\boldsymbol{y}}) T_n^*(\tilde{\boldsymbol{y}}) \tag{12}$$

with the underlying trigonmetric functions $T_n^*(\tilde{\boldsymbol{y}})$ defined as

$$T_n^*(\tilde{\boldsymbol{y}}) = \sin\left(\frac{\tilde{\boldsymbol{y}} \pi}{n} \right). \tag{13}$$

Corresponding bending and torsion modes for the wing case are also shown in Fig. 2. In contrast to the Chebyshev-based modes, gradients of the local surface deformation are significantly smaller towards the wing-tip.

2.4 Practical Implementation Details

The Flowsimulator framework [25] is used to efficiently couple CFD- and ROM-based aerodynamics with a CSM solver. High-fidelity CFD simulations are performed using the DLR-TAU code [26] solving the RANS equations in conjunction with the Spalart–Allmaras turbulence model [27] whereas ROM techniques are implemented in the DLR-SMARTy (Surrogate Modeling for Aero Data Toolbox in Python) toolbox [12, 18]. Structural analyses such as computing deformations and/or optimizing thicknesses are performed using the commercial software MSC Nastran™ [28]. Essential parameters of the fluid-structure coupling are summarized in Tab. 1. Moving least-squares splines are applied to transfer forces and displacements forth and back between the different solvers. Whereas this ensures a consistent work transfer, local forces get slightly smeared based on the number of basis points.

The DLR-TAU code is widely used in the European aerospace sector and validations of the code are available in the literature [26, 29, 30]. Since the proposed ROM provides results which are at best identical to the underlying coupled CFD-CSM simulations, results in this report are compared with their full-order model (FOM) counterparts rather than experimental data. However, an initial comparison to steady experimental results for the LANN wing are provided. Inviscid

Table 1: Numerical settings for coupled fluid-structure analysis which are equivalent for CFD- and ROM-based aerodynamics

	wing case	wing-body case
Maximum coupling iterations	10	50
Force convergence criterion	0.0001	0.002
Displacement convergence criterion	0.0001	0.005
Displacement relaxation factor	0.9	0.75
Moving least-squares basis points	200	500

fluxes are discretized applying a central scheme with the scalar artificial dissipation of Jameson, Schmidt and Turkel [31]. Exact gradients used for viscous and source terms are computed using the Green–Gauss approach. Solutions are obtained utilizing the backward Euler method with lower-upper Symmetric–Gauss–Seidel iterations [32] and local time-stepping. Convergence is accelerated by applying a 4v and 3v multigrid scheme for the wing and wing-body case, respectively. Parameters applied for solving the steady RANS equations can be found in Tab. 2. Note that, the maximum number of CFD iterations is given per CFD call and doubled for the wing-body case to ensure sufficient convergence. The density residual convergence criterion with $1e^{-6}$ is rather lenient since for the CFD-CSM simulations herein investigated this has been found sufficient.

Table 2: Numerical settings for full-order analysis

	wing case	wing-body case
CFL-number	2.0	2.0
Density residual convergence criterion	$1e^{-6}$	$1e^{-6}$
Maximum CFD iterations per CFD-call	2500	5000
Force convergence criterion	0.0001	0.0001

The POD modal basis computation uses a fully parallelized eigenvalue decomposition approach rather than an also available singular value decomposition. The surface deformation fit under force constraint minimization problem is solved using a sequential least square programming algorithm (SLSQP), parameters of which are given in Tab. 3. The vertical force constraint is considered as an equality constraint but could be converted into an inequality constraint by also defining an error region.

Table 3: Numerical settings for reduced-order analysis

	wing case	wing-body case
SLSQP convergence criterion	$1e^{-6}$	$1e^{-5}$
Maximum SLSQP iterations	100	100

3 RESULTS

This section presents results for a wing and a wing-body configuration to demonstrate the versatility of the proposed, shape-adaptive ROM. First, two different synthetic-mode basis-functions are compared and applied to predict forces and deformations on a wing while significantly altering the material stiffness. Secondly, for the wing-body case a structural optimization is performed within each fluid-structure coupling step which adjusts thicknesses to minimize weight while respecting a stress constraint. For both cases, results are compared with FOM solutions for aerodynamic as well as structural quantities of interest.

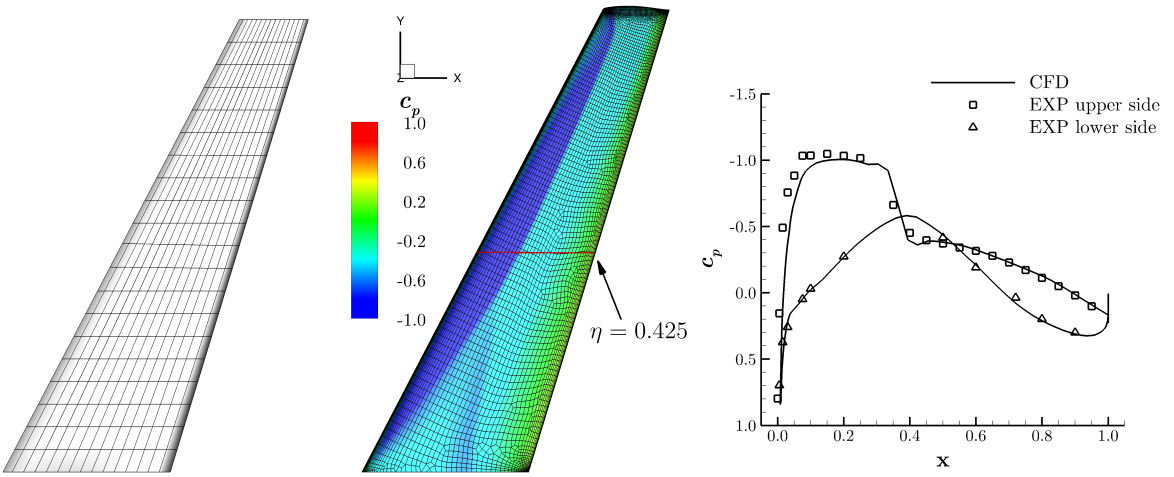

(a) CSM mesh

(b) CFD surface mesh and c_p distribution

(c) c_p at $\eta = 0.425$ in comparison to experimental data

Figure 3: Structural model, surface pressure distribution on the upper skin and c_p at a $\eta = 0.425$ in comparison to experimental data

Table 4: Flow conditions for the LANN-wing case

Parameter	Mach number	Reynolds number	Reference length
Value	0.82	7.3 x 10^6	0.3608 m

3.1 LANN-Wing Case

The first investigated test case is the LANN wing which was introduced from the AGARD group to analyze unsteady pitching phenomena [33]. Since no structural model is publicly available and the wing generally considered as infinitesimally stiff, an artificial model has been created by using solid elements with a constant stiffness. The resulting structural discretisation is displayed in Fig. 3(a). The applied computational aerodynamics mesh consists of 1.2 million points of which 22,500 are on the surface and is shown in Fig. 3(b). The investigated Mach number and Reynolds number are equivalent to the experimental case CT5 and given in Tab. 4 whereas the angle of attack is iteratively adjusted to match a target lift coefficient constraint. For validation purposes, the surface pressure distribution for a fixed angle of attack of 0.6 (equivalent to the CT5 case) is shown in Fig. 3(b) for the entire surface and in Fig. 3(c) for a selected slices at $\eta = 0.425$ in comparison to experimental measurements with good agreement and some minor deviations around the suction peak.

The initial step for the ROM construction is the computation of synthetic modes which are either based on trigonometric functions or Chebyshev polynomials with details given in Section 2.3. As a prerequisite an approximate elastic axis and the maximum wing-tip deflection as well as the maximum torsion angle needs to be defined. Even though these quantities might not be exactly known, a reasonable guess can be made at early stages of the design. For the LANN wing the approximated elastic axis is shown in Fig. 2 and correlates to the one-quarter chord length, the maximum wing-tip deflection is set to 15% of the wingspan and the torsion angle to 15° downwards. Two bending and two torsion modes are applied in the following (compare Fig. 2). More modes and hence higher degrees in the Chebyshev and trigonometric basis function have been tested but not found beneficial due to higher local gradients which are unphysical and/or negatively impact the sample generation. Note that, the bending, since it is computed around the elastic axis, also contains a torsion component.

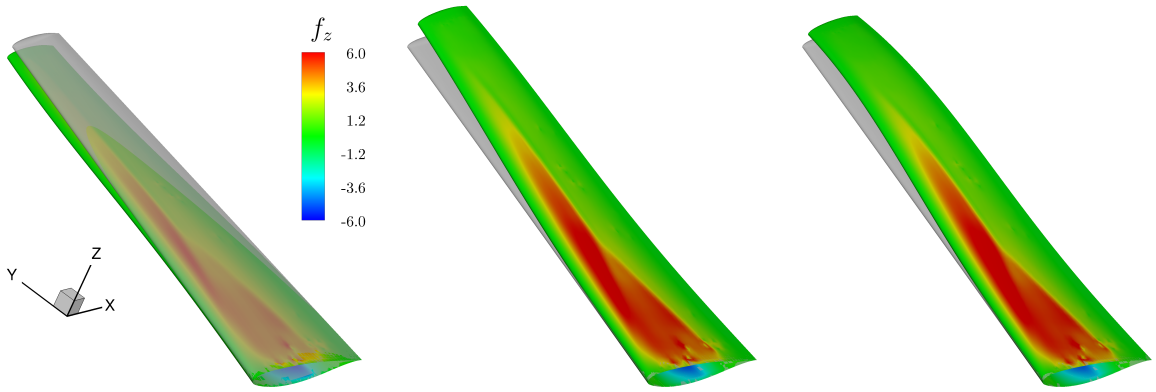

(a) Sample 1 (b) Sample 5 (c) Sample 10

Figure 4: Distributed vertical force $\boldsymbol{f_z}$ on deformed surface for three randomly selected samples using trigonometric modes. The undeformed surface is displayed as a reference in light grey.

Next, two separate ROMs are build to compare the different synthetic bases. For each ROM ten snapshots are computed using a Sobol sequence which defines the parameter combination at all sampling points. Since physical bounds are incorporated during the mode generation, the design of experiment is done within the bounds of -0.25 and 1 for all modes. In addition to the synthetic modes, the target lift coefficient is varied between 0.28 and 0.32 by the Sobol sequence enabling the ROM to adjust to changes in mass by increasing or decreasing the target vertical force. Resulting vertical surface deformations $\Delta \boldsymbol{c_z}$ and distributed vertical forces $\boldsymbol{f_z}$ for three randomly selected samples using a trigonometric function-based modal basis are displayed in Fig. 4. Obtained surface forces reflect common aeroelasticity knowledge of higher loading inboard while increasing wing-tip-deflection and torsion cause a decrease in forces outboard. Compared to the baseline surface pressure distribution in Fig. 3(b) the lambda-shock structure inboard has nearly disappeared once the wing bends upwards. Even though the imposed surface deformations differ from structurally driven displacements, the samples aim at covering the design space rather than point-matching expected deformations. Whereas this is clearly beneficial for deformations $\Delta \boldsymbol{c}$ because of their linear nature (this assumes that the underlying structural model is linear), the implications on the aerodynamic forces $\boldsymbol{f}$ is harder to quantify due to their highly nonlinear behaviour especially in the transonic flow regime. The relative information content for modal truncation which is applied during the ROM construction is set to $r_k = 0.999999$ resulting in 9 retained modes for both ROMs.

The predictive capabilities of both models are compared for three structural cases whereas for all of them a converged coupled fluid-structure solution is iteratively achieved (NASTRAN solution 101). First, the E-modulus of the wing material is set to $E = 7.0 \times 10^{10}$ which corresponds to aluminum. Differences to the FOM for surface deformations in z-direction and distributed vertical forces are displayed in Figs. 5(a) and 5(b) for the trigonometric- and Chebyshev-based ROM, respectively. Displacements are accurately predicted with small errors of below 0.2% of the chord length at around 30% span independent of the applied modal basis. Errors in vertical force are centered around the lambda-shock formation and are between -5% and 5% of the total force range. When reducing the E-modulus to $E = 3.5 \times 10^{10}$ the wing becomes more flexible and thus the maximum-wing tip deflection increases to roughly 5% of the wingspan. Whereas the trigonometric function-based ROM shows a similar accuracy for displacements and forces as for the previous, stiffer case the average displacement error for the Chebyshev-based ROM nearly doubles and some minor deviations at the wing-tip occur (compare Figs. 5(c) and 5(d)).

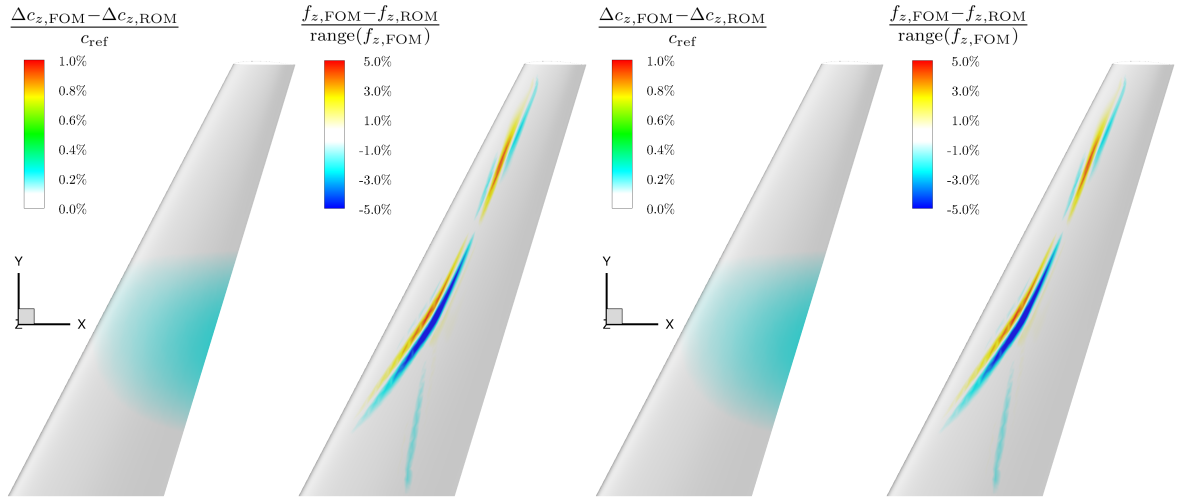

(a) Trigonometric modes with $E = 7.0 \times 10^{10}$

(b) Chebyshev modes with $E = 7.0 \times 10^{10}$

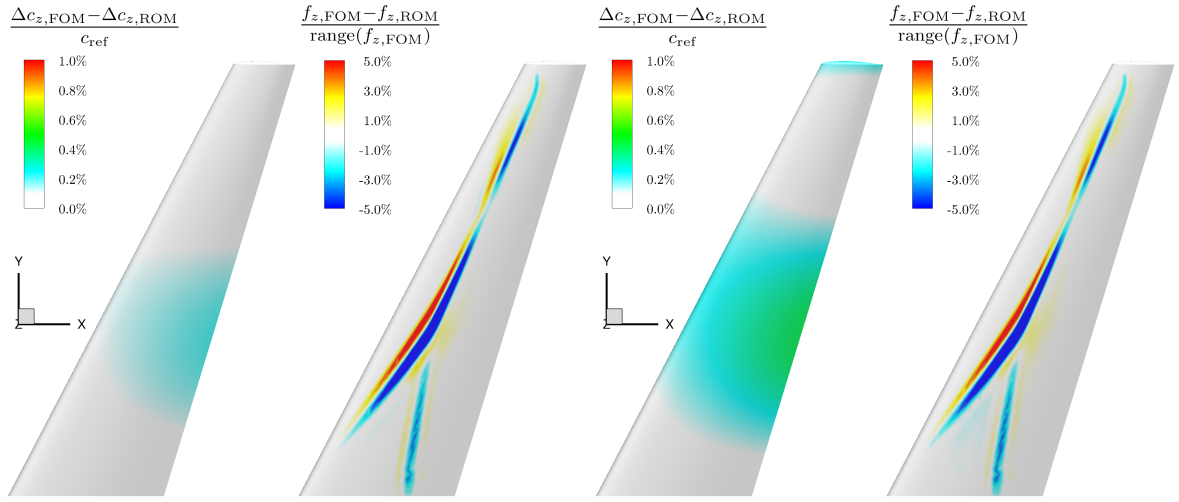

(c) Trigonometric modes with $E = 3.5 \times 10^{10}$

(d) Chebyshev modes with $E = 3.5 \times 10^{10}$

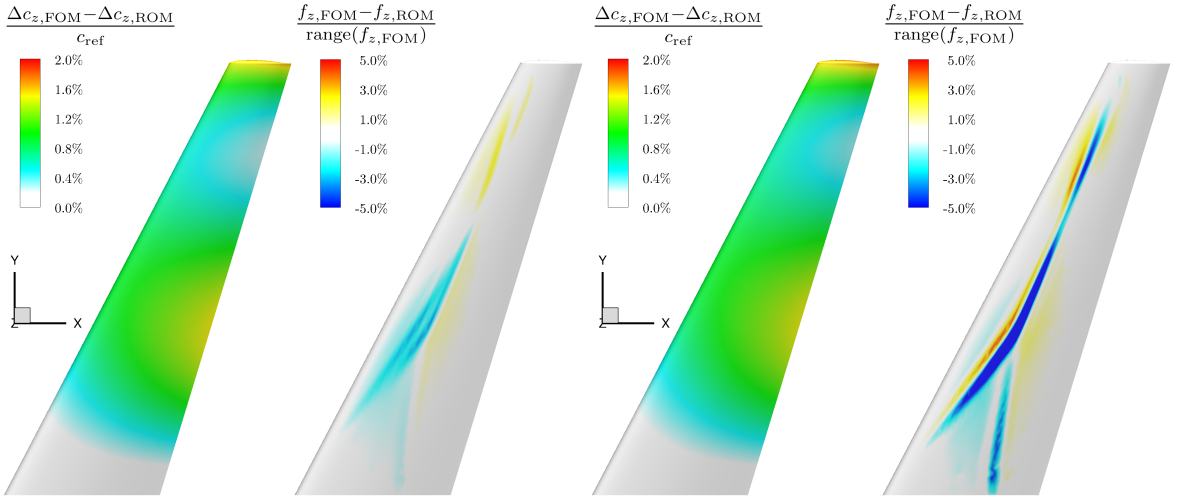

(e) Trigonometric modes with $E = 1.0 \times 10^{10}$

(f) Chebyshev modes with $E = 1.0 \times 10^{10}$

Figure 5: Comparison of FOM and ROM results of the LANN-wing case for different E-modulus E with respect to surface deformations and vertical forces for M=0.82 and Re=7.3 x 10^6

Table 5: Comparison of computational cost for the LANN-wing case

Model	Offline cost	Online cost	Cost E-modulus study
FOM	NA	7.5 h	22.5 h
ROM Trigonometric	10.0 h	0.2 h	0.6 h
ROM Chebyshev	10.5 h	0.2 h	0.6 h

When further decreasing the E-modulus to $E = 1.0 \times 10^{10}$, differences in surface deformations become more pronounced with values up to 1.8% of the chord length. For the trigonometric-based ROM the error for vertical forces in relation to the vertical force range decreases while for the Chebyshev-based ROM the error range remains nearly unchanged. Thus, the trigonometric function-based ROM performs slightly better than its Chebyshev counterpart.

Computational cost, split in an offline and online part, is given in hours in Tab. 5 for the FOM and both ROMs. Offline cost include the synthetic mode generation, the snapshots computation and the POD model forming while the online cost contain one coupled fluid-structure analysis and hence have a contribution of the structural solver. Since a CFD-CSM analysis is always online, the FOM-based coupling process does not have offline cost but rather high online cost with 7.5 h whereas both ROM-based coupling approaches are around 0.2 h which is primarily the time the structural solver needs. During the model construction roughly 10 h are necessary. Note that, herein, LANN-wing simulations which call for CFD evaluations are performed on a local 4-core system and the samples have been computed consecutively. However, all snapshots are unrelated and thus could be computed simultaneously if enough computational resources are available. In contrast, the CFD-CSM analysis is an iterative process which can not be easily parallelized. In conclusion, the proposed ROM offers computational benefits once more than one structural model is of interest at a fixed aerodynamic evaluation point as the cost for the E-modulus study highlights. When comparing both synthetic mode formulations, the trigonometric-based model slightly outperforms the Chebyshev-based model due to higher accuracy combined with reduced offline computational cost. Based on these observations only the trigonometric-based ROM while be applied for the wing-body configuration.

3.2 Long-Range Wing-Body Case

The second investigated case is the XRF1 wing-body configuration which is representative of a long-range, passenger aircraft with a semi-wingspan of 29.0 m. The XRF1 research test case is used by Airbus to engage with external partners on development and demonstration of relevant capabilities. The fuselage length-to-diameter ratio is about 11, the wing aspect ratio is about 8.5, the taper ratio is about 0.22 and the quarter-chord sweep angle is around 30°. The mean aerodynamic chord c_{ref} and the reference area are around 7.5 m and 380 m^2, respectively. The computational mesh with nearly 2.2 million points of which 45,000 are on the surface is shown in Fig. 6 in a three-view illustration. The mesh has been created ensuring a y-plus consistently below 1.0 for the herein investigated flow conditions. The analyzed flow cases are given in Tab. 6 and correlate to a 2.5g subsonic load-cases at sea-level and a 2.5g transonic load-case at an altitude of 6.1 km. Whereas the former defines the lower right corner of the flight envelope, the latter is given by the kink on the right-hand side of the envelope. The aircraft mass is consistently set to 245,000 kg which is equivalent to the maximum take-off weight. The mass is initially distributed such that the maximum number of payload is present and fuel is adjusted until maximum take-off weight is reached. The corresponding target lift coefficients used for CFD simulations are $C_{L,tar,LC1} \approx 0.74$ and $C_{L,tar,LC2} \approx 0.79$.

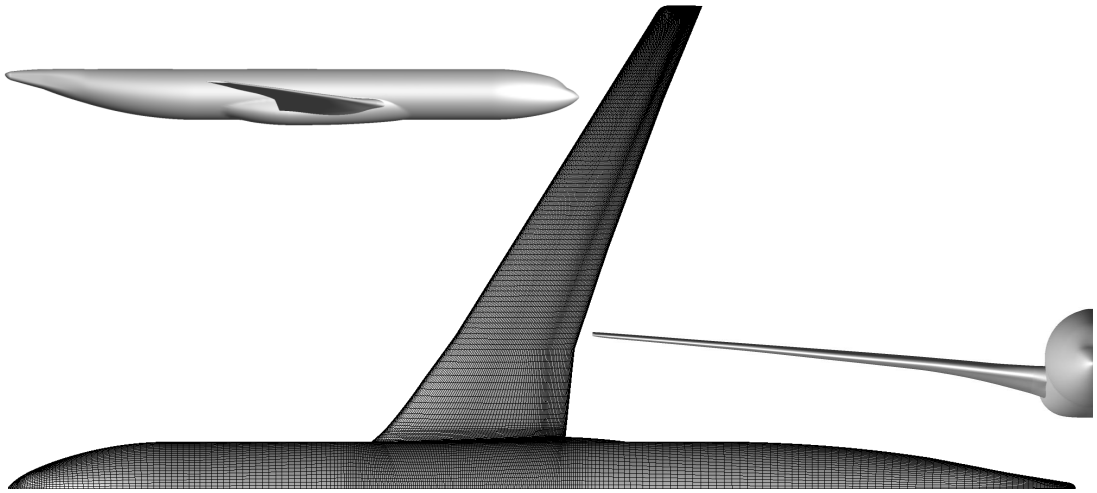

Figure 6: Three-view illustration of wing-body case with surface-mesh detail

Table 6: Load cases for the wing-body case

Load Case ID	LC1	LC2
Mach number	0.552	0.784
Altitude	0.0 km	6.1 km
Mass	245,000 kg	245,000 kg
Load-factor	2.5	2.5
Mass-case	MTOW	MTOW
Payload	100%	100%
Fuel-load	65%	65%

The structural model consists primarily out of quadrilateral plate element (Nastran CQUAD4 elements). The inner structure is displayed in Fig. 7(b) and contains the wing-box as well as ribs which connect leading and trailing edge. Shell elements on top and bottom of the wing box (compare Fig. 7(a) in blue) are modelled as aluminum and their thicknesses are adjusted during each fluid-structure coupling with the aim to minimize weight. During the optimization, von Mises stress values are used as constraints with a minimum of $-2.0e^8 \frac{N}{m^2}$ and a maximum of $2.0e^8 \frac{N}{m^2}$. Additional surface elements have been added around the leading and trailing edge to ensure a consistent force and displacement transfer between both subdisciplines. These elements have an artificial stiffness to transfer loads in chord direction to the wing box but not in span direction to avoid additional bending stiffness from leading and trailing edges. During the structural optimization these load transfer elements are kept unchanged. Secondary loads have been distributed around the wing-box as point forces to represent distributed fuel masses and the engine mass including pylon. For the structural optimization process Nastran solution 200 is utilized with a maximum of 50 iterations.

In an offline step two ROMs are constructed using 4 synthetic modes based on trigonometric functions each. Per model, 10 samples are computed while varying the target lift coefficient between 0.72 and 0.76 for LC1 and between 0.77 and 0.81 for LC2. The design of experiment is again done by a Sobol algorithm within the bound of -0.25 and 1.0 for all four modes. The elastic axis is estimated at one quarter of the chord length, maximum wing-tip deflection are set to $5\ m$ and a torsion of 15° downwards is used. Since the structural model currently only describes the wing structure, the synthetic modes are solely applied to this area and the fuselage

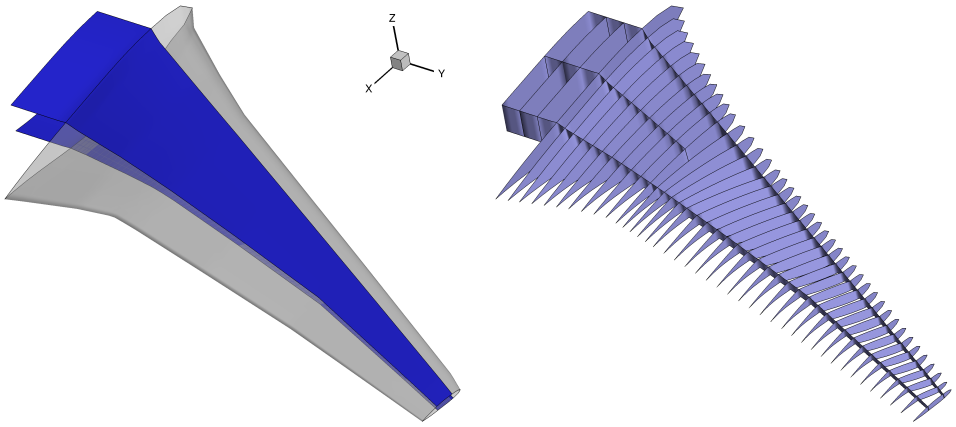

(a) Outer CSM mesh (b) Inner CSM mesh

Figure 7: Outer and inner CSM model with optimization areas highlighted in blue for the wing-body case. Grey outer shell elements are used for a consistent force and displacement transfer between aerodynamics and structure.

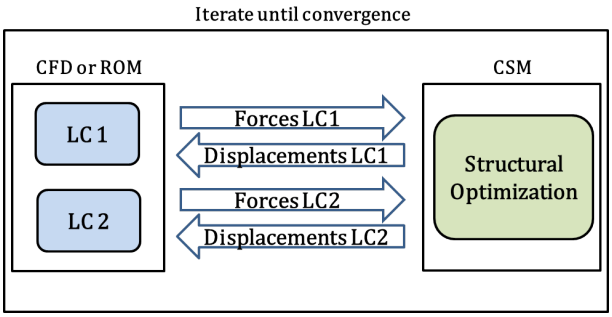

Figure 8: Schematic representation of a loosely coupled fluid-structure simulations framework

is assumed to be rigid. The ROMs are build by retaining 99.9999% of the relative information content resulting in 9 POD modes each.

A coupled fluid-structure analysis is performed using the ROMs and the aforementioned structural model. Within each iteration the structural model adjusts the thicknesses of the wing box shell to minimize weight without violating the von Mises stress constraint. A schematic representation of the workflow is given in Fig. 8. In each step, aerodynamic forces for case LC 1 and LC 2 are computer either using the CFD-solver or the corresponding ROM and then passed to Nastran to perform a structural analysis which includes an optimization. This iterative process is repeated until convergence for the relatives changes in forces and displacements is reached. Results are compared between the FOM- and ROM-based approach for the wing-deformation behaviour and two zooms around the wing-tip for both load cases in Fig. 9. The displayed result describes the converged solution of the outlined, iterative coupling process which has minimum weight while respecting the stress constraint and fulfilling the trimming constraint. The wing-tip deformation, independent of the aerodynamic modelling, is around 3.85 m and 3.94 m for LC 1 and 2, respectively. Whereas, no differences around the wing tip are visible for LC 1, the maximum difference at the wing tip for LC 2 is roughly 0.05 m with the ROM slightly over-predicting the FOM deformation. Hence, good agreement is observed between both simulation techniques. Note that, the structural model is evaluated by taking forces from both aerodynamic cases at the same time into account and thus occurring differences are always a result of all load cases simultaneously.

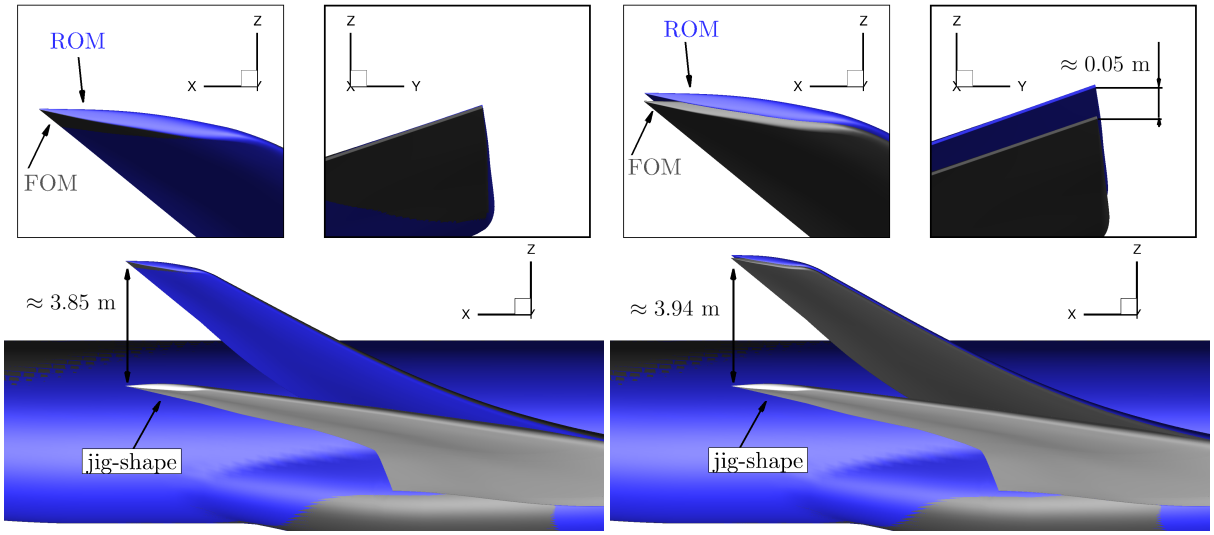

(a) Load case 1 at M=0.552, H=0.0 km (b) Load case 2 at M=0.784, H=6.1 km

Figure 9: Differences in surface deformation between FOM (grey) and ROM (blue) for the wing-body case

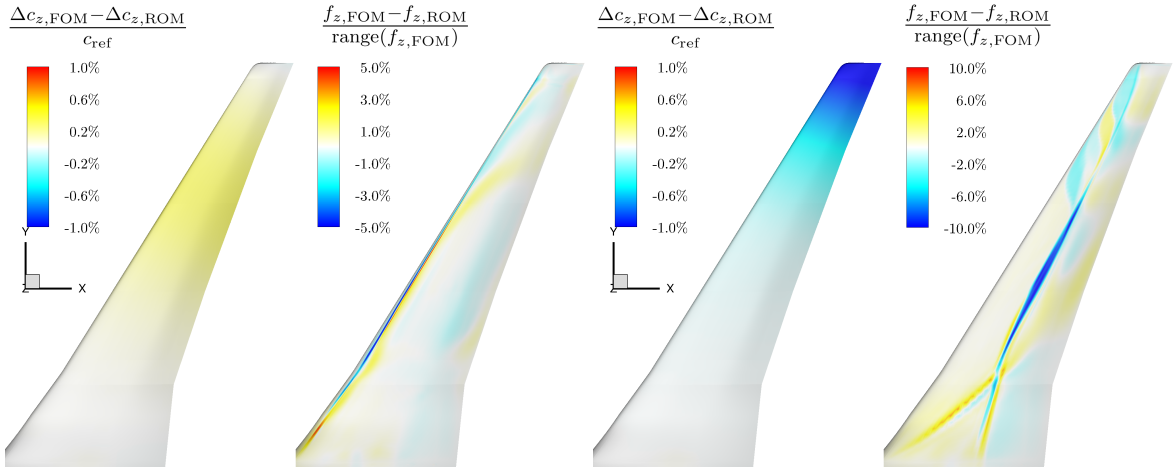

(a) Load case 1 at M=0.552, H=0.0 km (b) Load case 2 at M=0.784, H=6.1 km

Figure 10: Differences in vertical deflection $\Delta \boldsymbol{c_z}$ and vertical force $\boldsymbol{f_z}$ between FOM and ROM for the wing-body case

Final differences in percentage for vertical surface deformations $\Delta \boldsymbol{c_z}$ and vertical forces $\boldsymbol{f_z}$ after converging the coupled analysis are displayed in Fig. 10. With respect to vertical deformations, aforementioned global trends are confirmed from the more detailed analysis with barely no differences for LC 1 and maximum values around the wing-tip for LC 2. Differences in vertical force are primarily around the leading edge inboard for the subsonic case and around the shock location in the transonic case which has already previously been observed for the LANN wing. Due to the constrain on the total vertical force, the sum of these differences becomes zero. Moreover, the influence of these vertical force differences on the final deformed shape is negligible, even though values are quite large with approximately 6%.

Besides displacements and forces also final skin thicknesses are compared between both approaches. A comparison of thickness for each surface panel is shown in Fig. 11(a) and highlights good agreement between the FOM and ROM process with the ROM causing thicknesses to be slightly higher for panels around the engine-wing-pylon junction at both sides of the wing.

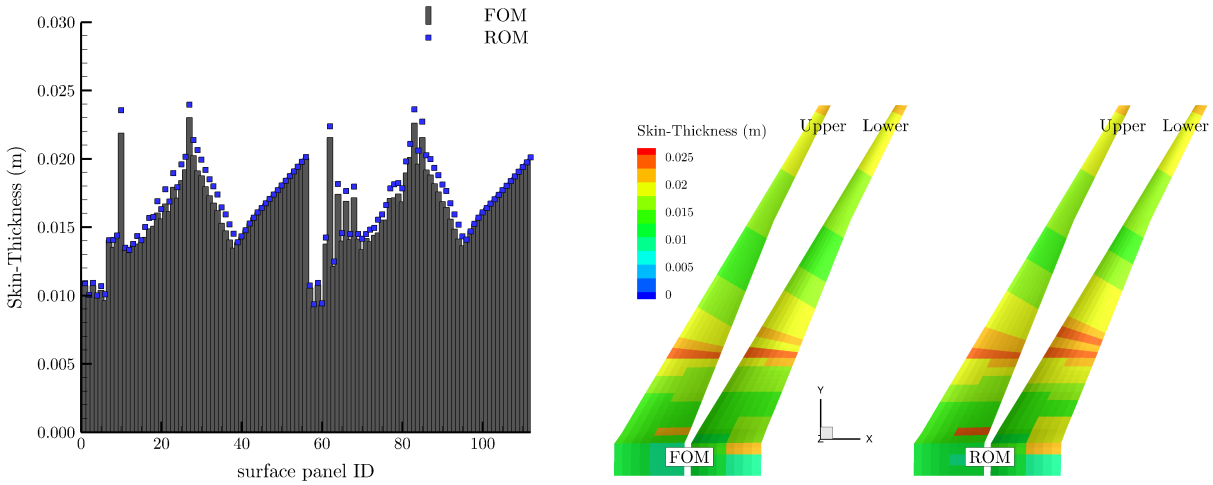

(a) Thicknesses per panel ID

(b) Distributed thicknesses

Figure 11: Skin thickness distribution for FOM and ROM of the wing-body case

Table 7: Comparison of computational cost for the wing-body case

Model	Offline cost	Online cost (2 LCs)	Online cost (4 LCs)
FOM	NA	≈360 CPUh	≈720 CPUh
ROM	≈420 CPUh	0.2 CPUh	0.3 CPUh

Currently only a stress constraint is used for structural optimization and thus thickness are not representative of an actual aircraft and are expected to increase once an additional buckling constraint is incorporated. Nevertheless, the defined test case serves as a benchmark for the proposed ROM methodology and the overall difference in wing mass is below 1% when co-marping both aerodynamic modeling strategies. When analyzing the thickness distributions on the upper and lower skin in more detail, displayed in Fig. 11(b), no significant differences are visible. Around the engine location, which is part of the structural model as a condensed mass-point, some minor discrepancies are visible. Since the aerodynamic model currently lacks an engine, the predicted forces within this area are inaccurate and hence a reliable statement on the ROM capabilities is postponed until an updated aerodynamic model is available.

Computational cost in CPUh are compared between the CFD-based analysis and the ROM-based approach in Table 7. As for the wing-case, the ROM cost are split in an offline and online contribution. Whereas the offline cost occurs once and primarily contains the sampling data generation on a high performance computing system, the online cost describes the coupled fluid-structure analysis which is performed locally. With just 0.2 CPUh this cost is significantly below the CFD-CSM based analysis and moreover, primarily dominated from the structural optimization using Nastran. The ROM part in percentage is roughly 20% and thus is below 3 min in total. Since the FOM-based analysis is always performed online on a high-performance computing system, no offline cost are given. Comparing the sum of offline and online cost, the ROM-based approach offers computational benefits once more than one structural model at a given flight point is of interest. Changes in the structural model might include a redistribution of secondary masses, altering the topology and/or changing the applied structural materials.

Next, computational benefits of the ROM-based approach are demonstrated by performing an additional coupled fluid-structure analysis with increased number of load cases as defined in

Table 8: Extended load cases for the wing-body case

Load Case ID	LC1	LC1.1	LC2	LC2.1
Mach number	0.552	0.552	0.784	0.784
Altitude	0.0 km	0.0 km	6.1 km	6.1 km
Mass	245,000 kg	245,000 kg	245,000 kg	245,000 kg
Load-factor	2.5	2.5	2.5	2.5
Mass-case	MTOW	MTOW	MTOW	MTOW
Payload	100%	84%	100%	84%
Fuel-load	65%	91%	65%	91%

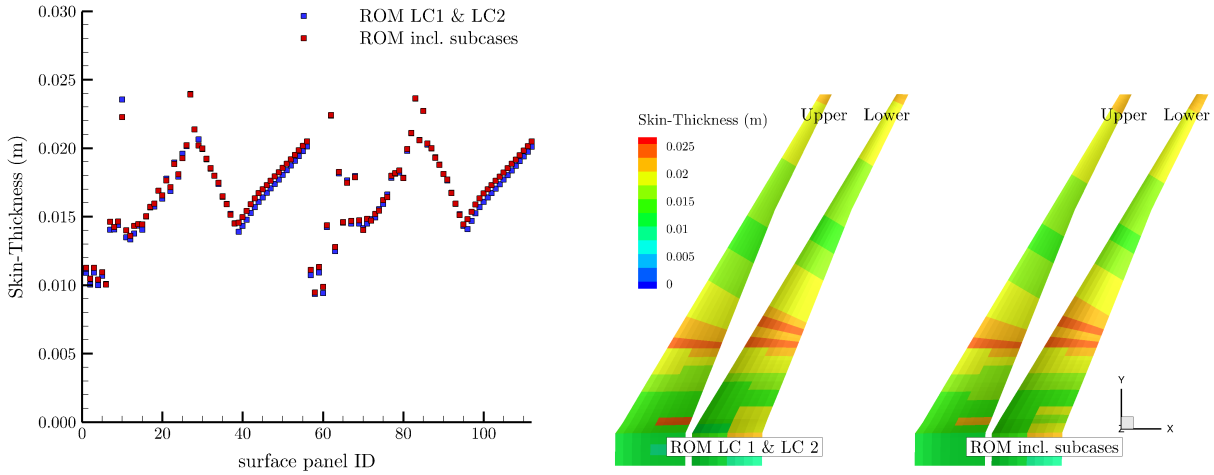

(a) Thicknesses per panel ID

(b) Distributed thicknesses

Figure 12: Skin thickness distribution for FOM and ROM of the wing-body case accounting for additional load cases

Table 8. Besides the already discussed cases LC 1 and LC 2 the cases LC 1.1 and LC 2.1 are added. These cases have the same aerodynamic parameters as their parental cases but secondary masses are distributed differently throughout the aircraft. The payload has been reduced to 84% whereas the fuel-load has been increased to 91%. The derived and already discussed ROMs for LC 1 and LC 2 can be used for the corresponding subcases at no additional cost.

A comparison of the final thickness per surface panel ID and the surface thickness distribution between the two and four load cases analysis is given in Fig. 12 showing only minor differences throughout the wing. The results labeled ROM LC 1 & LC 2 are equivalent to the previously discussed results in Fig. 11. With the additional load cases, slightly increased thickness values towards the wing-tip on both sides of the wing are occurring and again the engine-wing junction area on the lower-wing side is affected. When comparing computational cost, the ROM-based simulation was performed on a local desktop computer on a single core in just under 20 minutes whereas the full-order equivalent would have already taken days on a high-performance computing system (compare Table 7), clearly highlighting the computational benefit of the herein proposed ROM method for changing structural models.

4 CONCLUSIONS

This paper outlines a method of model order reduction to perform steady fluid-structure analysis at low computational cost while preserving the accuracy of the underlying computational fluid dynamics solver. Therefore, the concept of synthetic modes is pursued which is combined with proper orthogonal decomposition as order reduction technique. Surface forces to an arbitrary surface deformation are predicted by solving a small-sized minimization problem while constraining the summed vertical force to account for trimming conditions. The proposed reduced order model can than substitute a computational fluid dynamics analysis during coupled fluid-structure simulations and enables the analysis of varying structural models in a rapid fashion.

Results are presented for a wing and a wing-body test case at subsonic and transonic flow conditions. For the wing case two different synthetic mode functions are employed and the predictive capabilities of the corresponding reduced order models are compared to full-order simulations for displacements as well as forces. Throughout good agreement has been observed with the trigonometric function-based modes being slightly more accurate. For the wing-body case a structural optimization is performed within each iteration which adjusts shell thicknesses to minimize weight while respecting a von Mises stress constraint. Also for this complex case with altering structural model during each iteration, good agreement with the reference solution has been found indicating that the proposed model reduction technique offers a versatile model for steady fluid-structure analysis.

In a next step the model should be extended towards geometric parameter variations such as aspect ratio and wing span to enable its usage within a multidisciplinary optimization framework. In addition, the inclusion of a horizontal tail plane is currently investigated to perform a force as well as moment trimming by constrainting both degrees of freedom in the reduced order model. Moreover, surface force predictions could be enhanced further by utilizing a non-linear model reduction technique such as kernel principal component analysis or ISOMAP rather than proper orthogonal decomposition.

ACKNOWLEDGEMENTS

The authors would like to thank Airbus for providing the XRF1 test case as a mechanism for demonstration of the approaches presented in this paper.

5 REFERENCES

[1] Slotnick, J., Khodadoust, A., Alonso, J., et al. (2009). CFD Vision 2030 Study. In *A Path to Revolutionary Computational Aerosciences*. NASA/CR-2014-218178.

[2] Piperni, P., DeBlois, A., and Henderson, R. (2013). Development of a Multilevel Multidisciplinary-Optimization Capability for an Industrial Environment. *AIAA Journal*, 51(10), 2335–2352.

[3] Kenway, G. K. W. and Martins, J. R. R. A. (2014). Multipoint High-Fidelity Aerostructural Optimization of a Transport Aircraft Configuration. *Journal of Aircraft*, 51(1), 144–160.

[4] Wunderlich, T. and Dähne, S. (2017). Aeroelastic tailoring of an NLF forward swept wing. *CEAS Aeronautical Journal*, 8(3), 461–479.

[5] Görtz, S., Ilić, C., Abu-Zurayk, M., et al. (2016). Collaborative Multi-Level MDO Process Development and Application To Long-Range Transport Aircraft. In *30th Congress of the International Council of the Aeronautical Sciences (ICAS)*. ICAS 2016-0345.

[6] Achard, T., Blondeau, C., and Ohayon, R. (2018). High-Fidelity Aerostructural Gradient Computation Techniques with Application to a Realistic Wing Sizing. *AIAA Journal*, 56(11), 4487–4499.

[7] Ilić, C., Merle, A., Ronzheimer, A., et al. (2018). Cybermatrix: A novel approach to computationally and collaboration intensive multidisciplinary optimization for transport aircraft design. In *MSC's proceedings for 1999 Aerospace User's Conference*.

[8] Lucia, D. J., Beran, P. S., and Silva, W. A. (2004). Reduced-order modeling: new approaches for computational physics. *Progress in Aerospace Sciences*, 40(1-2), 51–117.

[9] Lumley, J. L. (1967). The Structures of Inhomogeneous Turbulent Flow. *Atmospheric Turbulence and Radio Wave Propagation*, 166–178.

[10] Sirovich, L. (1987). Turbulence and the dynamics of coherent structures, Parts I-III. *Q. Appl. Math.*, XLV, 561–590.

[11] Bui-Thanh, T., Damodaran, M., and Willcox, K. (2003). Proper orthogonal decomposition extensions for parametric applications in compressible aerodynamics. In *Proceedings of the 21st AIAA Applied Aerodynamics Conference*. Orlando, Florida: AIAA.

[12] Franz, T., Zimmermann, R., Görtz, S., et al. (2014). Interpolation-based Reduced-order Modeling for Steady Transonic Flows via Manifold Learning. *Special Issue: Reduced order modelling: the road towards real-time simulation of complex physics, International Journal of Computational Fluid Dynamics*, 28(3-4), 106–121.

[13] Fossati, M. (2015). Evaluation of Aerodynamic Loads via Reduced-Order Methodology. *AIAA Journal*, 53(8), 2389–2405.

[14] Ripepi, M., Verveld, M., Karcher, N., et al. (2018). Reduced Order Models for Aerodynamic Applications, Loads and MDO. *CEAS Aeronautical Journal*, 9(1), 171–193.

[15] Hall, K. C., Thomas, J. P., and Dowell, E. H. (2000). Proper Orthogonal Decomposition Technique for Transonic Unsteady Aerodynamic Flows. *AIAA Journal*, 38(10), 1853–1862.

[16] Amsallem, D., Cortial, J., and Farhat, C. (2010). Towards Real-Time Computational-Fluid-Dynamics-Based Aeroelastic Computations Using a Database of Reduced-Order Information. *AIAA Journal*, 48(9), 2029–2037.

[17] Bekemeyer, P., Thormann, R., and Timme, S. (2017). Rapid Gust Response Simulation of Large Civil Aircraft using Computational Fluid Dynamics. *The Aeronautical Journal*, 121(1246), 1795–1807.

[18] Zimmermann, R. and Görtz, S. (2010). Non-linear reduced order models for steady aerodynamics. *Procedia Computer Science*, 1(1), 165–174.

[19] Bekemeyer, P., Ripepi, M., Heinrich, R., et al. (2019). Nonlinear Unsteady Reduced Order Models based on Computational Fluid Dynamics for Gust Loads Predictions. *AIAA Journal*, 57(5), 1839–1850.

[20] Bisplinghoff, R. L., Ashley, H., and Halfman, R. L. (1955). *Aeroelasticity*. Dover Publications.

[21] Voss, R., Tichy, L., and Thormann, R. (2011). A ROM based Flutter Prediction Process and its Validation with a New Reference Model. In *International Forum on Aeroelasticity and Structural Dynamics*. IFASD-2011-36.

[22] Zhang, W., Chen, K., and Ye, Z. (2015). Unsteady aerodynamic reduced-order modeling of an aeroelastic wing using arbitrary mode shapes. *Journal of Fluids and Structures*, 58(0889-9746), 254 – 270.

[23] Winter, M., Heckmeier, F. M., and Breitsamter, C. (2017). CFD-based aeroelastic reduced-order modeling robust to structural paramter varations. *Aerospace Sciene and Technology*, 67, 13–30.

[24] Holmes, P., Lumley, J. L., Berkooz, G., et al. (2012). *Turbulence, coherent structures, dynamical systems and symmetry*. Cambridge Univ. Press, 2nd ed.

[25] Reimer, L. (2015). The FlowSimulator - A software framework for CFD-related multidisciplinary simulations. In *European NAFEMS Conference Computational Fluid Dynamics (CFD) – Beyond the Solve*.

[26] Schwamborn, D., Gerhold, T., and Heinrich, R. (2006). The DLR TAU-Code: Recent Applications in Research and Industry. In *European Conference on Computational Fluid Dynamics*. ECCOMAS CFD 2006.

[27] Spalart, P. R. and Allmaras, S. R. (1994). A One-Equation Turbulence Model for Aerodynamic Flows. *Recherche Aerospatiale*, 1, 5–21.

[28] MSC.Software Corporation. *MSC Nastran 2012 Linear Static Analysis User's Guide*. MSC.Software.

[29] Neumann, J. and Mai, H. (2013). Gust response: Simulation of an Aeroelastic Experiment by a Fluid-Structure Interaction Method. *Journal of Fluids and Structures*, 38, 290–302.

[30] Stickan, B., Dillinger, J., and Schewe, G. (2014). Computational aeroelastic investigation of a transonic limit-cycle-oscillation experiment at a transport aircraft wing model. *Journal of Fluids and Structures*, 49, 223–241.

[31] Jameson, A., Schmidt, W., and Turkel, E. (1981). Numerical Solutions of the Euler Equations by Finite Volume Methods Using Runge-Kutta Time-Stepping Schemes. In *14th Fluid and Plasma Dynamic Conference*. AIAA Paper 1981–1259.

[32] Dwight, R. (2006). An Implicit LU-SGS Scheme for Finite-Volume Discretizations of the Navier-Stokes Equations on Hybrid Grids. *DLR-FB-2005-05*.

[33] Zwaan, I. R. J. (1982). LANN Wing Pitching Oscillations. In *Compendium of Unsteady Aerodynamic Measurements, AGARD-R-702 Addendum No. 1*, August.

COPYRIGHT STATEMENT